

Marc O. Delchini^a, Jean C. Ragusa^{*,a}, Ray A. Berry^b

^a*Department of Nuclear Engineering, Texas A&M University, College Station, TX 77843, USA*

^b*Idaho National Laboratory, Idaho Falls, ID 83415, USA*

Abstract

aaa

Key words: aaa, bbb, ccc

1. Introduction

Over the past years an increasing interest raised for computational methods that can solve both compressible and incompressible flows. In engineering applications, there is often the need to solve for complex flows where a near incompressible regime or low Mach flow coexists with a supersonic flow domain. For example, such flow are encountered in aerodynamic in the study of airships. In the nuclear industry, flows are nearly the incompressible regime but compressible effects cannot be neglected because of the heat source and thus needs to be accurately resolved.

When solving the multi-D Euler equations for a wide range of Mach numbers, multiple problems have to address: stability, accuracy and acceleration of the convergence in the low Mach regime. Because of the hyperbolic nature of the equations, shocks can form during transonic and supersonic flows, and require the use of the numerical methods in order to stabilize the scheme and correctly resolve the discontinuities. The literature offers a wide range of stabilization methods: flux-limiter, pressure-based viscosity method, Lapidus method, the entropy-viscosity method among others. These numerical methods are usually tested and developed using simple equation of states and for transonic and supersonic flows where the disparity between the acoustic waves and the fluid speed is not large since the Mach number is of order one. This approach leads to a well-known accuracy problem in the low Mach regime where the fluid velocity is smaller than the speed of sound by multiple order of magnitude. The numerical dissipative terms become ill-scaled in the low Mach regime, Because of the hyperbolic nature of the flow equations, numerical methods are

*Corresponding author

Email addresses: `delchmo@tamu.edu` (Marc O. Delchini), `jean.ragusa@tamu.edu` (Jean C. Ragusa), `ray.berry@inl.gov` (Ray A. Berry)

required in order to accurately resolve shocks that can form during transonic and supersonic flows. Numerous numerical methods are available in the literature: flux-limiter, pressure-based viscosity method, Lapidus method, the entropy-viscosity method among others. This approach often leads to issues in the low Mach regime where the fluid velocity is smaller by multiple order of magnitude.

$$\begin{cases} \partial_t(\rho) + \vec{\nabla} \cdot (\rho \vec{u}) = 0 \\ \partial_t(\rho \vec{u}) + \vec{\nabla} \cdot (\rho \vec{u} \otimes \vec{u} + P \mathbf{I}) = 0 \\ \partial_t(\rho E) + \vec{\nabla} \cdot [\vec{u}(\rho E + P)] = 0 \\ P = P(\rho, e) \end{cases} \quad (1)$$

where ρ , $\rho \vec{u}$ and ρE are the density, the momentum and the total energy, respectively, and will be referred to as the conservative variables. The pressure P is computed with an equation of state expressed in function of the density ρ and the specific internal energy e . The tensor product $\vec{a} \otimes \vec{b}$ is taken with the following convention: $(\vec{a} \otimes \vec{b})_{i,j} = a_i b_j$. Lastly, the terms ∂_t , $\vec{\nabla}$, $\vec{\nabla} \cdot$ and \mathbf{I} denote the temporal derivative, the gradient and divergent operators, and the identity tensor, respectively.

2. The Entropy Viscosity Method

2.1. Background

In this section, the entropy-based viscosity method [1, 2, 3] is recalled for the multi-D Euler equations (with constant area A) [4]. As mentioned in Section 1 the entropy-based viscosity method consists of adding dissipative terms, with a viscosity coefficient modulated by the entropy production which allows high-order accuracy when the solution is smooth. Thus, two questions arise: (i) how are the viscosity dissipative terms derived and (ii) how to numerically compute the entropy production. Answers to the first question can be found in [5] by Guemond et al., that details the proof leading to the derivation of the artificial dissipative terms (Eq. (2)) consistent with the entropy minimum principle theorem. The viscous regularization obtained is valid for any equation of state as long as the opposite of the physical entropy function, s , is convex with respect to the internal energy e and the specific volume $1/\rho$. As for the entropy production, it is locally evaluated by computing the local entropy residual $D_e(\vec{x}, t)$ defined in Eq. (4), that is peaked in shocks.

$$\begin{cases} \partial_t(\rho) + \vec{\nabla} \cdot (\rho \vec{u}) = \vec{\nabla} \cdot (\kappa \vec{\nabla} \rho) \\ \partial_t(\rho \vec{u}) + \vec{\nabla} \cdot (\rho \vec{u} \otimes \vec{u} + P \mathbf{I}) = \vec{\nabla} \cdot (\mu \rho \vec{\nabla}^s \vec{u} + \kappa \vec{u} \otimes \vec{\nabla} \rho) \\ \partial_t(\rho E) + \vec{\nabla} \cdot [\vec{u}(\rho E + P)] = \vec{\nabla} \cdot (\kappa \vec{\nabla}(\rho e) + \frac{1}{2} \|\vec{u}\|^2 \kappa \vec{\nabla} \rho + \rho \mu \vec{u} \vec{\nabla} \vec{u}) \\ P = P(\rho, e) \end{cases} \quad (2)$$

where κ and μ are local positive viscosity coefficients. $\vec{\nabla}^s \vec{u}$ denotes the symmetric gradient operator that guarantees the method to be rotational invariant

[5].
 In the current version of the method, κ and μ are set equal, so that the above viscous regularization (Eq. (2)) is equivalent to the parabolic regularization [6] when considering the 1-D form of the equation. The current definition includes a first-order viscosity coefficient referred to with the subscript max , and a high-order viscosity coefficient referred to with the subscript e . The first-order viscosity coefficients μ_{max} and κ_{max} are proportional to the local largest eigenvalue $||\vec{u}|| + c$ and equivalent to an upwind-scheme (see Eq. (3)), when used, which is known to be over-dissipative and monotone [7]:

$$\mu_{max}(\vec{r}, t) = \kappa_{max}(\vec{r}, t) = \frac{h}{2} (||\vec{u}|| + c), \quad (3)$$

where h is defined as the ratio of the grid size to the polynomial order of the test functions used.

The second-order viscosity coefficients κ_e and μ_e are set proportional to the entropy production that is evaluated by computing the local entropy residual D_e . It also includes the interfacial jump of the entropy flux J that will allow to detect any discontinuities other than shocks:

$$\mu_e(\vec{r}, t) = \kappa_e(\vec{r}, t) = h^2 \frac{\max(|D_e(\vec{r}, t)|, J)}{||s - \bar{s}||_\infty} \text{ with } D_e(\vec{r}, t) = \partial_t s + \vec{u} \cdot \vec{\nabla} s \quad (4)$$

where $||\cdot||_\infty$ and $\bar{\cdot}$ denote the infinite norm operator and the average operator over the entire computational domain, respectively. The definition of the jump J is discretization-dependent and examples of definition can be found in [4] for DGFEM. The denominator $||s - \bar{s}||_\infty$ is used for dimensionality purposes and should not be of the same order as h , on penalty of loosing the high-order accuracy. Currently, there are no theoretical justification for choosing the denominator.

The definition of the viscosity coefficients μ and κ is function of the first- and second-order viscosity coefficients as follows:

$$\mu(\vec{r}, t) = \min(\mu_e(\vec{r}, t), \mu_{max}(\vec{r}, t)) \text{ and } \kappa(\vec{r}, t) = \min(\kappa_e(\vec{r}, t), \kappa_{max}(\vec{r}, t)). \quad (5)$$

This definition allows the following properties. In shock regions, the second-order viscosity coefficient experiences a peak because of entropy production, and thus, saturates to the first-order viscosity that is known to be over-dissipative and will smooth out oscillations. Anywhere else, the entropy production being small, the viscosity coefficients μ and κ are of order h^2 .

Using the above definition of the entropy-based viscosity method, high-order accuracy was demonstrated and excellent results were obtained with 1-D Sod shock tubes and various 2-D tests [1, 2, 4].

2.2. Issues in the Low-Mach Regime

In the Low-Mach Regime, the flow is known to be isentropic resulting in very little entropy production. Since the entropy viscosity method is directly

91 based on the evaluation of the local entropy production, it will be interested
 92 to study how the entropy viscosity coefficients μ and κ scale in the low Mach
 93 regime. Mathematically, it means that the entropy residual D_e will be very
 94 small, so will be the denominator $\|s - \bar{s}\|_\infty$, thus making the ratio, used in
 95 the definition of the viscosity coefficients Eq. (4), undetermined. Therefore, the
 96 current definition of the viscosity coefficients seems unadapted to subsonic flow
 97 and could lead to ill-scaled dissipative terms. A solution would be to recast
 98 the entropy residual as a function of other variables in order to have more
 99 freedom in the choice of the normalization parameter. With this approach, the
 100 viscosity coefficients are still defined proportional to the entropy residual that
 101 is a good indicator of the flow type (subsonic, transonic and supersonic flow).
 102 Plus, a different normalization parameter could be chosen, based on a low Mach
 103 asymptotic study so that the viscosity coefficients are well-scaled in the low
 104 Mach asymptotic limit (see Section 3).

105 *2.3. The dissipative-terms for the multi-D Euler equations with variable area*

106 One of the focus of this paper is to investigate the application of the entropy
 107 viscosity method to the multi-D Euler equations with variable area. The variable
 108 area version of the Euler equations is mostly used in 1-D and 2-D for obvious
 109 reasons, and differs from Eq. (1) by the momentum equation as shown in Eq. (6),
 110 that contains a non-conservative term proportional to the area gradient. For the
 111 purpose of this paper, the variable area is assumed to be a smooth function and
 112 only spatial dependent. An example can be found in (REF) where a fluid flows
 113 through a 1-D convergent-divergent nozzle and reaches a steady-state solution.

$$\begin{cases} \partial_t (\rho A) + \vec{\nabla} \cdot (\rho \vec{u} A) = 0 \\ \partial_t (\rho \vec{u} A) + \vec{\nabla} \cdot [A (\rho \vec{u} \otimes \vec{u} + P \mathbf{I})] = P \vec{\nabla} A \\ \partial_t (\rho E) + \vec{\nabla} \cdot [\vec{u} (\rho E + P)] = 0 \end{cases} \quad (6)$$

114 The application of the entropy viscosity method to the above system of equa-
 115 tions is expected to be straightforward since it degenerates to the Eq. (1) when
 116 assuming a constant area. Details of the derivations of the dissipative terms
 117 are available to the reader in APPENDIX and are very similar to what was
 118 done in [5]: an entropy residual is derived without the dissipative terms. Then,
 119 the same entropy residual is re-derived after adding dissipative terms to each
 120 equation of the system given in Eq. (6), and the entropy minimum principle is
 121 used as a condition to obtain a definition for each of the dissipative terms. The
 122 final result including the dissipative terms is given in Eq. (7):

$$\begin{cases} \partial_t (\rho A) + \vec{\nabla} \cdot (\rho \vec{u} A) = \vec{\nabla} \cdot (A \kappa \vec{\nabla} \rho) \\ \partial_t (\rho \vec{u} A) + \vec{\nabla} \cdot [A (\rho \vec{u} \otimes \vec{u} + P \mathbf{I})] = P \vec{\nabla} A + \vec{\nabla} \cdot \left[A \left(\mu \rho \vec{\nabla}^s \vec{u} + \kappa \vec{u} \otimes \vec{\nabla} \rho \right) \right] \\ \partial_t (\rho E) + \vec{\nabla} \cdot [\vec{u} (\rho E + P)] = \vec{\nabla} \cdot \left[A \left(\kappa \vec{\nabla} (\rho e) + \frac{1}{2} \|\vec{u}\|^2 \kappa \vec{\nabla} \rho + \rho \mu \vec{u} \vec{\nabla} \vec{u} \right) \right] \end{cases} \quad (7)$$

123 The dissipative terms are very similar to the ones obtained for the multi-D Euler
 124 equations: each dissipative flux is multiplied by the variable area A in order to

125 ensure conservation of the flux. When assuming a constant area, Eq. (2) is
 126 retrieved. The definition of the viscosity coefficients μ and κ is explained in
 127 Section 3.2.

128 3. All-speed Reformulation of the Entropy Viscosity Method

129 In this section, it is shown how the entropy residual D_e can be recast as a
 130 function of the pressure, the density and the speed of sound. Then, a low Mach
 131 asymptotic study of the multi-D Euler equations is performed in order to derive
 132 the correct normalization parameter.

133 3.1. New Entropy Production Residual

134 The first step in defining a viscosity coefficient that behaves well in the low
 135 mach limit is to recast the entropy residual in terms of the thermodynamic
 136 variables as shown in Eq. (8):

$$D_e(\vec{r}, t) = \partial_t s + \vec{u} \cdot \vec{\nabla} s = \frac{s_e}{P_e} \left(\underbrace{\frac{dP}{dt} - c^2 \frac{d\rho}{dt}}_{\tilde{D}_e(\vec{r}, t)} \right), \quad (8)$$

137 where $\frac{d}{dt}$ denotes the material or total derivative, and P_e is the partial derivative
 138 of pressure with respect to internal energy. The steps that lead to the new
 139 formulation of the entropy residual D_e can be found in APPENDIX.
 140 The entropy residual D_e and \tilde{D}_e are proportional to each other and therefore
 141 will experience the same variation when taking the absolute value. Thus, locally
 142 evaluating \tilde{D}_e instead of D_e should allow us to measure the entropy production
 143 point wise. This new expression given in Eq. (8) has multiple advantages:

- 144 • an analytical expression of the entropy function is not longer needed: the
 145 entropy residual \tilde{D}_e is evaluated using the local values of the pressure, the
 146 density and the speed of sound. Deriving an entropy function for some
 147 complex equation of states can be difficult.
- 148 • with the proposed expression of the entropy residual function of pressure
 149 and density, additional normalizations suitable for low Mach flows of the
 150 entropy residual can be devised. Examples include the pressure itself,
 151 or combination of the density, the speed of sound and the norm of the
 152 velocity: ρc^2 , $\rho c ||\vec{u}||$ and $\rho ||\vec{u}||^2$.

153 The viscosity coefficients μ and κ are now defined proportional to the new
 154 entropy residual \tilde{D}_e on the model of Eq. (4) as follows:

$$\mu(\vec{r}, t) = \kappa(\vec{r}, t) = h^2 \frac{\max(\tilde{D}_e, J)}{n(P)} \quad (9)$$

155 where $n(P)$ is a normalization parameter to determine and all other variables
 156 were defined previously.
 157 As mentioned earlier, the normalization parameter $n(P)$ must be of the same
 158 units as the pressure for the viscosity coefficients to have the unit of a dy-
 159 namic viscosity (m^2/s). Multiples options are available to us (P , ρc^2 , $\rho c||\vec{u}||$
 160 and $\rho||\vec{u}||^2$). The choice of the normalization parameter cannot be random if
 161 the definition of the viscosity coefficient is wanted to be well-scaled for a wide
 162 range of Mach numbers. For example, by choosing $n(P) = \rho||\vec{u}||^2$, the viscosity
 163 coefficient will become very large as the Mach number decreases which would
 164 be unnecessary since the equations will not develop any shock or discontinuity.
 165 Therefore, it is proposed to carry, in Section 3.2, a low-Mach asymptotic study
 166 of the multi-D Euler equations in order to determine the correct expression for
 167 the normalization parameter $n(P)$.

168 3.2. Low-Mach asymptotic study of the multi-D Euler equations

169 The asymptotic study requires the multi-D Euler equations to be non di-
 170 mensionalized: the objective is to make the Mach number appears and thus,
 171 use a polynomial expansion of the variables as a function of the Mach number
 172 in order to derive the leading, first- and second-order equations. Before detailing
 173 the steps of the asymptotic method, let us have a closer look at the system of
 174 equations under consideration. The initial system of equations is composed of
 175 the multi-D Euler equations. For stability purpose, artificial dissipative terms
 176 are added to each equation as explained in Section 2. The resulting system of
 177 equations is alike the multi-D Navier-Stokes equations in a sense that it con-
 178 tains second-order derivative terms. Thus, it would be interesting to look at
 179 the steps employed in the asymptotic study of the multi-D Navier-Stokes equa-
 180 tions in order to understand how the dissipative terms are treated. Fortunately,
 181 this process is well-documented in the literature (REFS) for both multi-D Eu-
 182 ler equations and Navier-Stokes equations. The work presented here is mainly
 183 inspired of (REF) that focuses on the asymptotic study in the low Mach regime
 184 of Navier-Stokes equations. During the derivation, the reader has to keep in
 185 mind that the objective of this section is to derive a normalization parameter
 186 for the definition of the viscosity coefficients so that the multi-D Euler equa-
 187 tions degenerate to the incompressible system of equations, which implies that
 188 the dissipative terms are well-scaled. The full derivation that leads to the final
 189 result can be found in APPENDIX. In this section, only the main steps are
 190 recalled.

191 To express Eq. (2) in dimensionless variables, the following definitions are used

$$\begin{aligned}
 \rho &= \frac{\rho^*}{\rho_\infty}, P = \frac{P^*}{\rho_\infty c_\infty^2}, \mu = \frac{\mu^*}{\mu_\infty}, E = \frac{E^*}{c_\infty^2}, \mu = \frac{\mu^*}{\mu_\infty}, \\
 \kappa &= \frac{\kappa^*}{\kappa_\infty}, x = \frac{x^*}{L_\infty}, t = \frac{t^*}{L_\infty/u_\infty}, u = \frac{u^*}{u_\infty}
 \end{aligned} \tag{10}$$

192 where the subscript ∞ and the upper script $*$ denote far field or stagnation
 193 quantities and the dimensionless variables, respectively. The reference quantities

are chosen such that the non dimensional flow quantities are of order one for any low reference-Mach number

$$M_\infty = \frac{u_\infty^*}{c_\infty^*} \quad (11)$$

where c_∞^* is a reference value for the speed of sound. Then, using the non dimensional quantities and the multi-D Euler equations from Eq. (2), the following non dimensional form is obtained:

$$\begin{cases} \partial_t \rho + \nabla \cdot (\rho \vec{u}) = \frac{1}{Re_\infty Pr_\infty} \nabla \cdot (\kappa \nabla \rho) \\ \partial_t (\rho \vec{u}) + \nabla \cdot (\rho \vec{u} \otimes \vec{u}) + \frac{1}{M_\infty^2} \nabla (P) = \frac{1}{Re_\infty} \nabla \cdot (\rho \mu \nabla \vec{u}) + \frac{1}{Re_\infty Pr_\infty} \nabla \cdot (\vec{u} \otimes \kappa \nabla \rho) \\ \partial_t (\rho E) + \nabla \cdot [\vec{u} (\rho E + P)] = \frac{1}{Re_\infty Pr_\infty} \nabla \cdot (\kappa \nabla (\rho e)) + \frac{M_\infty^2}{Re_\infty} \nabla \cdot (\vec{u} \rho \mu \nabla \vec{u}) \\ + \frac{M_\infty^2}{2 Re_\infty Pr_\infty} \nabla \cdot (\kappa u^2 \nabla \rho) \\ P = (\gamma - 1) (\rho E + M_\infty^2 \rho u^2) \end{cases}$$

where the *numerical* Reynolds (Re_∞) and Prandtl (Pr_∞) numbers are defined as follows:

$$Re_\infty = \frac{u_\infty L_\infty}{\mu_\infty} \text{ and } Pr_\infty = \frac{\mu_\infty}{\kappa_\infty}. \quad (12)$$

Since it is chosen to have the same definition for both μ and κ the numerical Prandtl number is unconditionally equal to one: $Pr_\infty = 1$. Once the dimensionless equations are obtained, the next step consists of expanding each variable in term of the Mach number (example given in Eq. (13) for the pressure P) in order to derive the leading, first- and second-order equations.

$$P(\vec{r}, t) = P_0(\vec{r}, t) + P_1(\vec{r}, t)M_\infty + P_2(\vec{r}, t)M_\infty^2 + \dots \text{ with } M_\infty \rightarrow 0 \quad (13)$$

Before deriving the leading-order equation, a choice needs to be made on how the numerical Reynolds number scales. Multiple options are available to us and a few example are given: $Re_\infty = M_\infty$, or $Re_\infty = M_\infty^{-1}$ or $Re_\infty = 1$. Let us assume for academy purpose that the numerical Reynolds number scales as the inverse of the Mach number square: $Re_\infty = M_\infty^{-2}$. The best way to evaluate the impact of this choice on the equations, is to look at the momentum equation and try to derive the order M_∞^{-2} :

$$\vec{\nabla} P_0 = \vec{\nabla} \cdot (\rho_0 \mu_0 \vec{\nabla} \vec{u}_0 + \vec{u}_0 \otimes \vec{\nabla} \rho_0) \quad (14)$$

which is known to be (REF)

$$\vec{\nabla} P_0 = 0 \quad (15)$$

It is clear that Eq. (14) and Eq. (15) will not yield the same result. The same conclusion is drawn when deriving the order M_∞^{-1} of the momentum equation, making our initial assumption not suitable. From the above result, it is understood that the numerical Reynolds number has to scale as one so that it does

not affect the orders M_∞^{-2} and M_∞^{-1} of the momentum equations: $Re_\infty = 1$.
Thus, with such assumption, Eq. (12) implies:

$$\begin{aligned}
& \text{At order } M_\infty^{-2}: \\
& \quad \vec{\nabla} P_0 = 0 \\
& \text{At order } M_\infty^{-1}: \\
& \quad \vec{\nabla} P_1 = 0 \\
& \text{At leading-order:} \\
& \quad \partial_t \rho_0 + \vec{\nabla} \cdot (\rho_0 \vec{u}_0) = \vec{\nabla} \cdot (\kappa_0 \vec{\nabla} \rho_0) \\
& \quad \partial_t (\rho_0 \vec{u}_0) + \vec{\nabla} \cdot (\rho_0 \vec{u}_0 \otimes \vec{u}_0) + \vec{\nabla} P_2 = \vec{\nabla} \cdot (\rho_0 \mu_0 \vec{\nabla} \vec{u}_0 + \vec{u}_0 \otimes \vec{\nabla} \rho_0) \\
& \quad \partial_t (\rho_0 E_0) + \vec{\nabla} \cdot [\vec{u}_0 (\rho_0 E_0 + P_0)] = \vec{\nabla} \cdot (\kappa_0 \vec{\nabla} (\rho_0 e_0))
\end{aligned}$$

Under this form, the dissipative terms are well-scaled and should not alter the physical solution in the asymptotic limit.
It is now determined that the numerical Reynolds number Re_∞ has to scale as one. Following Eq. (12), Re_∞ is a function of the μ_∞ , and thus n_P . It can be shown using Eq. (10) and the definitions of \tilde{D} given in Eq. (8) that:

$$\mu_\infty = \frac{\rho_\infty c_\infty^2 u_\infty L}{n_{P,\infty}} \quad (16)$$

where $n_{P,\infty}$ is the far-field quantity for the normalization parameter n_P . Substituting Eq. (16) into Eq. (12) and remembering that the numerical Reynolds number scales as one, it yields:

$$n_{P,\infty} = \rho_\infty c_\infty^2 \quad (17)$$

Eq. (17) tells us that in the asymptotic limit, the normalization parameter n_P scales as $\rho_\infty c_\infty^2$ which leaves us with two options: either $n_P = \rho c^2$ or $n_P = P$. The choice was made to use $n_P = \rho c^2$ in the asymptotic limit (it was found to behave well as shown in Section 5) which, we believe, is more representative of the flow type. This definition is only valid in the asymptotic limit and the purpose of this paper is to define a viscosity coefficient μ that is valid for a wide range of Mach numbers. Thus, it is proposed to define the high-order viscosity coefficient μ_e as follows:

$$\mu_e = h^2 \frac{\max(\tilde{D}_e, J)}{(1 - f(M))\rho c^2 + f(M)\rho ||\vec{u}||^2} \quad (18)$$

where $f(M)$ is a function of the local Mach number M with the following properties:

$$\begin{cases} f(M) \rightarrow 0 \text{ as } M \rightarrow 0 \\ f(M) \rightarrow 1 \text{ as } M \geq 1 \end{cases} \quad (19)$$

The choice of the function $f(M)$ is not fixed and a few examples are available in the literature. (REF) proposed the simple definition $f(M) = \min(M, 1)$ which

meets the conditions of Eq. (19). Another definition for $f(M)$ was proposed by (REF):

$$f(M) = \quad (20)$$

All of the numerical results presented in Section 5 were obtained by using $f(M) = \min(M, 1)$ which is simple to implement. A convergence test for a subsonic flow over a 2-D cylinder will show that this definition of $f(M)$ yields the correct behavior in the asymptotic limit. The definition of the high-order viscosity coefficient $\mu_e(\vec{r}, t)$ should behave well for complex flow where a near incompressible regime coexists with a supersonic flow domain since $f(M)$ is function of the local Mach number.

For clarity purpose, the full definition of the viscosity coefficient $\mu(\vec{r}, t)$ is recalled:

$$\begin{cases} \mu(\vec{r}, t) = \max(\mu_{max}(\vec{r}, t), \mu_e(\vec{r}, t)) \\ \text{where } \mu_{max}(\vec{r}, t) = \frac{h}{2}(\|\vec{u}\| + c) \\ \text{and } \mu_e(\vec{r}, t) = h^2 \frac{\max(\tilde{D}_e, J)}{(1-f(M))\rho c^2 + f(M)\rho\|\vec{u}\|^2} \\ \mu(\vec{r}, t) = \kappa(\vec{r}, t) \end{cases} \quad (21)$$

These viscosity coefficients are valid for both the multi-D Euler equations with variable and constant area and are employed with the dissipative terms detailed in Eq. (12). The reader will notice that, through the derivation, none assumption was made on the type of equation of state besides the convexity condition on the entropy function s . The remaining of this paper (Section 5) will focus on demonstrating that the definition of the viscosity coefficient given in Eq. (21) is indeed well-scaled in the asymptotic limit and that shocks are still well resolved.

4. Solution Techniques Spatial and Temporal Discretizations

In order to detail the partial and temporal discretization used for this study, the system of equations Eq. (7) is considered under the following form for simplicity:

$$\partial_t U + \vec{\nabla} \cdot F(U) = S \quad (22)$$

where U is the vector solution, F is a conservative vector flux and S is a vector source that can contain some relaxation source terms and non-conservative terms.

4.1. Spatial and Temporal Discretizations

The system of equation given in Eq. (22) is discretized using a continuous Galerkin finite element method and high-order temporal integrators provided by the MOOSE framework.

4.1.1. CFEM

In order to apply the continuous finite element method, Eq. (22) is multiplied by a smooth test function ϕ , integrated by part and each integral is split onto

each finite element e of the discrete mesh Ω bounded by $\partial\Omega$, to obtain a weak solution:

$$\sum_e \int_e \partial_t U \phi - \sum_e \int_e F(U) \cdot \vec{\nabla} \phi + \int_{\partial\Omega} F(U) \vec{n} \phi - \sum_e \int_e S \phi = 0 \quad (23)$$

The integrals over the elements e are evaluated using quadrature-point rules. The Moose framework provides a wide range of test function and quadrature rules: trapezoidal and Gauss rules among others. Linear Lagrange polynomials will be used as test functions and should ensure second-order convergence for smooth functions. The order of convergence will be demonstrated.

4.1.2. Temporal integrator

The MOOSE framework offers both first- and second-order explicit and implicit temporal integrators. In all of the numerical examples presented in Section 5, the time-dependent term $\int_e \partial_t U \phi$ will be evaluated using the second-order temporal integrator BDF2. By considering three converged solutions, U^{n-1} , U^n and U^{n+1} at three different time t^{n-1} , t^n and t^{n+1} , respectively, it yields:

$$\begin{aligned} \int_e \partial_t U \phi &= \int_e (\omega_0 U^{n+1} + \omega_1 U^n + \omega_2 U^{n-1}) \phi \\ \text{with } \omega_0 &= \frac{2\Delta t^{n+1} + \Delta t^n}{\Delta t^{n+1} (\Delta t^{n+1} + \Delta t^n)}, \\ \omega_1 &= -\frac{\Delta t^{n+1} + \Delta t^n}{\Delta t^{n+1} \Delta t^n} \\ \text{and } \omega_2 &= \frac{\Delta t^{n+1}}{\Delta t^n (\Delta t^{n+1} + \Delta t^n)} \end{aligned} \quad (24)$$

where $\Delta t^n = t^n - t^{n-1}$ and $\Delta t^{n+1} = t^{n+1} - t^n$.

4.2. Boundary conditions

The boundary conditions will be treated by either using Dirichlet or Neumann conditions. The multi-D Euler equations are wave-dominated systems that require great care when dealing with boundary conditions. It is often recommended to use the characteristic equations to compute the correct flux at the boundaries. Our implementation of the boundary conditions will follow the method described in [8] that was developed for Ideal Gas and Stiffened Gas equation of states. For each numerical solution presented in Section 5, the type of boundary conditions used will be specified: supersonic inlet, subsonic inlet (stagnation pressure boundary), supersonic outlet and subsonic inlet (static pressure boundary).

4.3. Solver

A Free-Jacobian-Newton-Krylov (FJNK) method is used to solve for the solution at each time step. The jacobian matrix of the discretized equations

was derived by hand, hard coded and used as a preconditioner. This method requires the partial derivative of the pressure with respect to the conservative variables to be known. The contribution of the artificial dissipative terms to the jacobian matrix is simplified by assuming constant viscosity coefficients as shown in Eq. (25) for the dissipative terms of the continuity equation:

$$\frac{\partial}{\partial U_i} \left(\kappa \vec{\nabla} \rho \vec{\nabla} \phi \right) = \kappa \frac{\partial}{\partial U_i} (\rho) \vec{\nabla} \phi \quad (25)$$

where U_i denotes the set of conservative variables.

5. Numerical Results

This section is dedicated to presenting 1- and 2-D numerical results obtained by solving Eq. (7) with the entropy viscosity method. This section has two objectives: validate our new definition of the viscosity coefficients for the low Mach limit, and, make sure that the new definition can still resolve shocks.

The first set of 1-D simulations consist of liquid water and steam flowing in a convergent-divergent nozzle. This test is interesting for multiple reasons: a steady-state is reached (some stabilization methods are known to have difficulties to reach a steady-state (REF)), it can be performed for liquid and gas phases, and, an analytical solution of the steady-state solution is available which allow for convergence study. The 1-D Leblanc shock tube test (REF) (in a straight pipe) is also performed (REF) and consists of a flow developing shocks. A convergence study will be performed in order to demonstrate convergence of the numerical solution to the exact solution.

This section also included 2-D simulations from subsonic to supersonic flows. Subsonic flows of a gas over a 2-D cylinder and a hump are simulated and results are shown for various far-field Mach numbers. Numerical results of a supersonic flow in a compression corner are provided to illustrate the capabilities of the new definition in the supersonic case. Convergence studies are performed when an analytical solution is available.

For each simulation, informations relative to the boundary conditions and the equation of state will be provided. All of the numerical solution presented in this section are run with the second-order temporal integrator *BDF2* and linear polynomials test functions. The integrals are numerically computed using a second-order Gauss quadrature rule.

The numerical results presented in Section 5 are all run using either the Ideal Gas or Stiffened Gas equation of state (REF). A generic formulation is recalled in Eq. (26).

$$P = (\gamma - 1)\rho(e - q) - \gamma P_\infty \quad (26)$$

where the parameters q and P_∞ are fluid dependent and will be specified in time. Eq. (26) degenerates to the Ideal Gas equation of state by setting q and P_∞ to zero. The Ideal and Stiffened Gas equation of states have a convex entropy s (REF):

$$s = C_v \ln \left(\frac{P + P_\infty}{\rho^{\gamma-1}} \right)$$

338 *5.1. Liquid water in a 1-D divergent-convergent nozzle*

339 The simulation consists of liquid water flowing through a 1-D convergent-
340 divergent nozzle with the following equation, $A(x) = 1 + 0.5 \cos(2\pi x/L)$, where
341 $L = 1m$ is the length of the nozzle. At the inlet, the stagnation pressure and
342 temperature are set to $P_0 = 1MPa$ and $T_0 = 453K$, respectively. At the outlet,
343 only the static pressure is specified: $P_s = 0.5MPa$. Details about the theory
344 related to the inlet and outlet boundary conditions can be found in (REFS).
345 Initially, the temperature is uniform and set equal to the stagnation temperature
346 and the pressure linearly decreases from the stagnation pressure to the static
347 one. Finally, the liquid is assumed at rest. The Stiffened Gas equation of state
348 is used to model the liquid water with the parameters provided in Table 1.

Table 1: Stiffened Gas Equation of State parameters for liquid water.

γ	$C_v (J \cdot kg^{-1} \cdot K^{-1})$	$P_\infty (Pa)$	$q (J \cdot kg^{-1})$
2.35	1816	10^9	-1167.10^3

349 Because of the low pressure difference between the inlet and the outlet,
350 and the large value of P_∞ , the flow remains subsonic and thus, should not
351 display any shock. Enthalpy and entropy are conserved through the nozzle, and
352 these conservation relations are used to determine the exact solution at steady-
353 state (REF). Plots of the velocity, density and pressure are given at steady-
354 state in Fig. 1a, Fig. 1b, Fig. 1c, respectively, along with the exact solution for
355 comparison. The viscosity coefficients are also plotted in Fig. 1d. The mesh
356 used is uniform and has 50 cells.

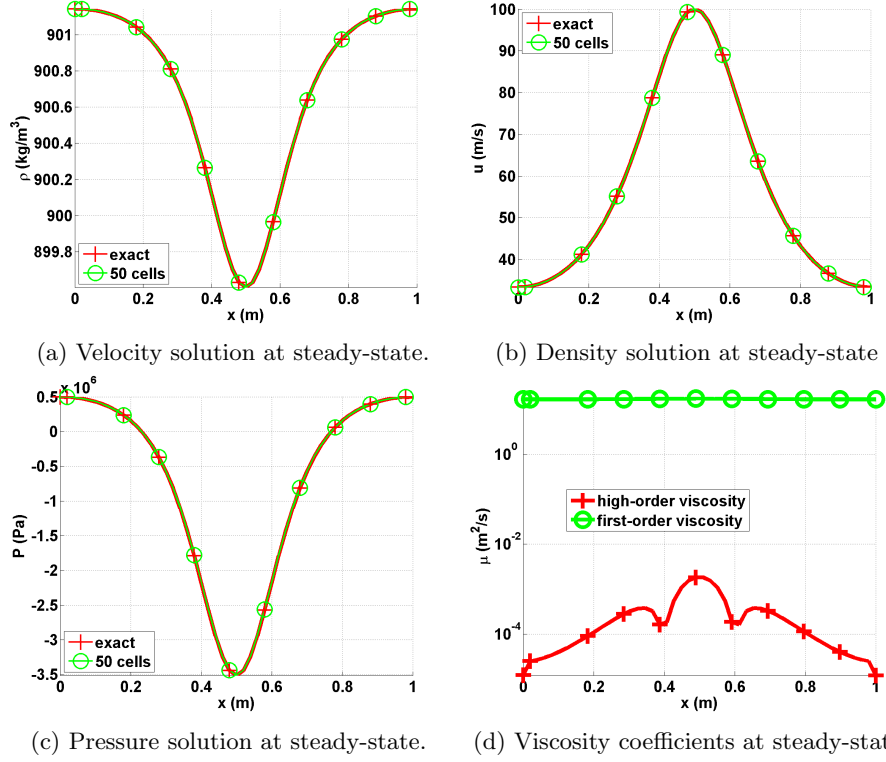


Figure 1: Steady-state solution for liquid phase in a 1-D convergent-divergent nozzle with an uniform mesh of 50 cells.

357 The numerical and exact solutions of the velocity, pressure and density given
 358 in Fig. 1 for a fairly coarse mesh (50 cells) perfectly overlap: it is noted that
 359 the numerical solution is symmetric with respect to the nozzle throat located
 360 in $x = 0.5m$. The second-order viscosity coefficient is very small compare to
 361 the first-order one as expected: (i) the numerical solution is smooth as shown
 362 in Fig. 1d and (ii) the flow is in a low Mach regime and thus isentropic . A
 363 convergence study was performed using the exact solution as a reference: the
 364 L1 and L2 norms of the error and the corresponding convergence rates are
 365 computed at steady-state on various uniform mesh from 4 to 256 cells. The
 366 results for linear polynomials Q_1 are reported in Table 2 and Table 3 for the
 367 primitive variables: density, velocity and pressure.

Table 2: L1 norm of the error for the liquid phase in a 1-D convergent-divergent nozzle at steady-state.

cells	density	rate	pressure	rate	velocity	rate
4	$2.8037 \cdot 10^{-1}$	—	$8.4705e \cdot 10^5$	—	7.2737	—
8	$1.3343 \cdot 10^{-1}$	1.0713	$4.7893e \cdot 10^5$	0.24227	6.1493	0.074683
16	$2.9373 \cdot 10^{-2}$	2.1835	$1.0613e \cdot 10^5$	2.3247	1.2275	2.4501
32	$5.1120 \cdot 10^{-3}$	2.5225	$1.8446 \cdot 10^4$	2.6959	$1.8943 \cdot 10^{-1}$	3.0966
64	$1.0558 \cdot 10^{-3}$	2.2755	$3.7938 \cdot 10^3$	2.3207	$3.7919 \cdot 10^{-2}$	2.3323
128	$2.3712 \cdot 10^{-4}$	2.1547	$8.4471 \cdot 10^2$	2.0624	$8.5517 \cdot 10^{-3}$	2.0473
256	$5.6058 \cdot 10^{-5}$	2.0806	$1.9839 \cdot 10^2$	2.0478	$2.0475 \cdot 10^{-3}$	1.9833
512	$1.3278 \cdot 10^{-5}$	2.0778	46.622	2.0478	$4.9516 \cdot 10^{-4}$	1.9669

Table 3: L2 norm of the error for the liquid phase in a 1-D convergent-divergent nozzle at steady-state.

cells	density	rate	pressure	rate	velocity	rate
4	$3.106397 \cdot 10^{-1}$	—	$5.254445 \cdot 10^5$	—	3.288543	—
8	$7.491623 \cdot 10^{-2}$	2.07	$1.636966 \cdot 10^5$	1.60	1.823880	0.90
16	$2.079858 \cdot 10^{-2}$	1.80	$4.627338 \cdot 10^4$	1.75	$4.990605 \cdot 10^{-1}$	1.83
32	$5.329627 \cdot 10^{-3}$	1.90	$1.180287 \cdot 10^4$	1.92	$1.261018 \cdot 10^{-1}$	1.93
64	$1.341583 \cdot 10^{-3}$	1.94	$2.967104 \cdot 10^3$	1.98	$3.160914 \cdot 10^{-2}$	1.99
128	$3.359766 \cdot 10^{-4}$	1.99	$7.428087 \cdot 10^2$	1.99	$7.907499 \cdot 10^{-3}$	1.99
256	$8.403859 \cdot 10^{-5}$	1.99	$1.857861 \cdot 10^2$	1.99	$1.977292 \cdot 10^{-3}$	1.99
512	$2.10075 \cdot 10^{-5}$	1.99	27.048	1.99	$4.9516 \cdot 10^{-4}$	1.99

It is observed that the convergence rate for the L1 and L2 norm of the error is 2: the entropy viscosity method conserves the high-order accuracy when the numerical solution is smooth, and the new definition of the entropy viscosity coefficient seems to behave as expected in the low Mach limit.

5.2. Steam in a 1-D divergent-convergent nozzle

Instead of liquid water, we now simulate a flow of steam using the exact same 1-D geometry, initial conditions and boundary conditions as in Section 5.1. The Stiffened gas equation of state is still used but with different parameters that are given in Table 4: steam is a gas and compressible effects will become dominant.

Table 4: Stiffened Gas Equation of State parameters for steam.

γ	$C_v \text{ (} J \cdot kg^{-1} \cdot K^{-1} \text{)}$	$P_\infty \text{ (Pa)}$	$q \text{ (} J \cdot kg^{-1} \text{)}$
1.43	1040	0	$2030 \cdot 10^3$

377 The pressure difference applied between the inlet and outlet is large enough
 378 to make the steam accelerates through the nozzle and result in the formation of
 379 shock in the divergent part. The behavior is different from what is observed for
 380 the liquid water phase in Section 5.1 because of the liquid to gas density ratio
 381 that is of 1000. Even though a shock forms, an exact solution at steady-state
 382 is still available (REF). The objective of this section is to show that using the
 383 new definition of the viscosity coefficient in Eq. (21), the shock can be correctly
 384 resolved without spurious oscillation. The steady-state numerical solution is
 385 shown in Fig. 2 and was run with a mesh of 1600 cells.

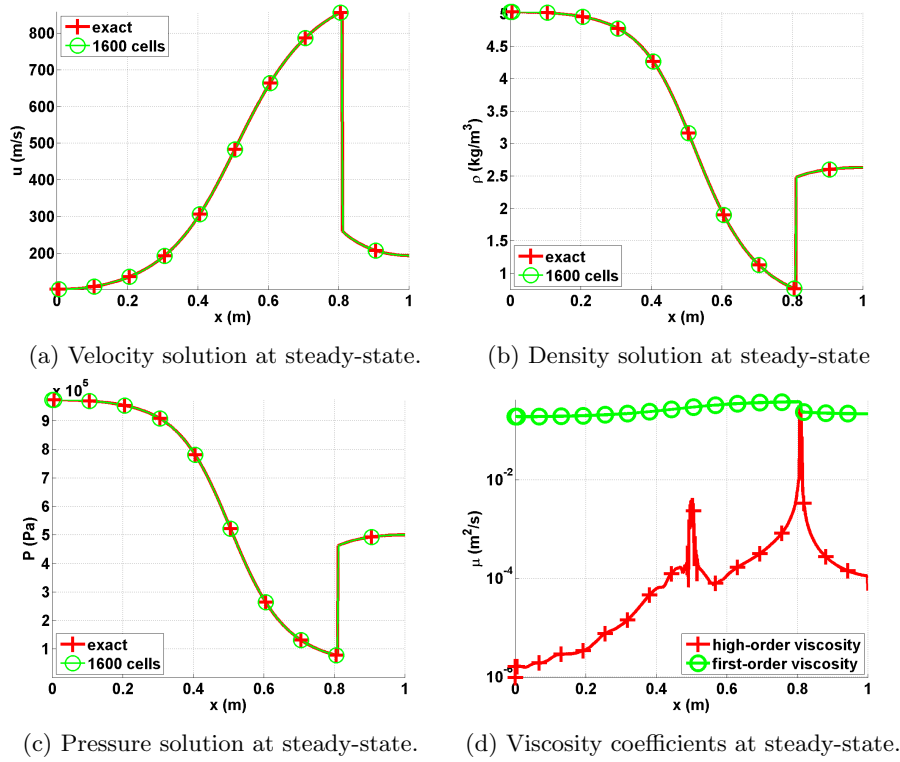


Figure 2: Steady-state solution for vapor phase in a 1-D convergent-divergent nozzle.

386 The steady-state solution of the density, velocity and pressure are given
 387 in Fig. 2a, Fig. 2b and Fig. 2c. The steady-solution displays a shock around
 388 $x = 0.8m$ and match the exact solution. In Fig. 2d, the first- and second-order
 389 viscosity coefficients are log plotted at steady-state: the second-order viscosity
 390 coefficient is peaked in the shock region around $x = 0.8m$ as expected, and
 391 saturate to the first-order viscosity coefficient. The profile also displays another
 392 peak at $x = 0.5m$ that corresponds to the position of the sonic point for a 1-

393 D convergent-divergent nozzle: this particular point is known to develop small
 394 instabilities that are detected when computing the jumps of the pressure and
 395 density gradients. Anywhere else, the second-order viscosity coefficient is small.
 396 In order to prove convergence of the numerical solution to the exact solution,
 397 a convergence study is performed. Because of the presence of a shock, second-
 398 order accuracy cannot be achieved. However, the convergence rate is known
 399 and expected to be of 1 and 1/2 when computing the L1 and L2 norms of the
 400 error, respectively. Results are reported in Table 5 and Table 6 for the primitive
 401 variables: density, velocity and pressure.

Table 5: L1 norm of the error for the vapor phase in a 1-D convergent-divergent nozzle at steady-state.

cells	density	rate	pressure	rate	velocity	rate
5	$0.72562 \cdot 10^{-1}$	—	$1.5657 \cdot 10^5$	—	173.69	—
10	$0.4165 \cdot 10^{-1}$	0.80088	$9.6741 \cdot 10^4$	0.63425	120.69	0.52519
20	$0.20675 \cdot 10^{-1}$	1.0104	$4.9193 \cdot 10^4$	0.96971	72.149	0.74228
40	$0.093703 \cdot 10^{-1}$	1.1417	$2.0103 \cdot 10^4$	0.72728	34.716	1.0554
80	$0.047328 \cdot 10^{-1}$	0.9854	$1.0208 \cdot 10^4$	0.9777	16.082	1.1101
160	$0.023965 \cdot 10^{-2}$	0.9817	$5.1969 \cdot 10^3$	0.9739	7.9573	1.0150
320	$0.020768 \cdot 10^{-2}$	0.9886	$2.5116 \cdot 10^3$	1.0490	3.7812	1.0734
640	$0.0059715 \cdot 10^{-2}$	1.0160	$1.2754 \cdot 10^3$	0.9776	1.8353	1.0428

Table 6: L2 norm of the error for the vapor phase in a 1-D convergent-divergent nozzle at steady-state.

cells	density	rate	pressure	rate	velocity	rate
5	$9.7144 \cdot 10^{-1}$	—	$2.0215 \cdot 10^5$	—	236.94	—
10	$5.9718 \cdot 10^{-1}$	0.70195	$1.3024 \cdot 10^5$	0.63425	166.56	0.50854
20	$2.9503 \cdot 10^{-1}$	1.0173	$6.6503 \cdot 10^4$	0.96971	103.36	0.68831
40	$1.8193 \cdot 10^{-1}$	0.69747	$4.0171 \cdot 10^4$	0.72728	66.374	0.6390
80	$1.3366 \cdot 10^{-1}$	0.44485	$2.3163 \cdot 10^4$	0.43576	42.981	0.62692
160	$9.6638 \cdot 10^{-2}$	0.46790	$1.7263 \cdot 10^4$	0.42413	31.717	0.43844
320	$7.0896 \cdot 10^{-2}$	0.44688	$1.2763 \cdot 10^4$	0.43571	23.138	0.45499
640	$5.2191 \cdot 10^{-2}$	0.44190	$9.4217 \cdot 10^3$	0.43790	16.910	0.45238

402 The convergence rates for the L1 and L2 norms of the error are close to
 403 the theoretical values which prove convergence of the numerical solution to the
 404 exact solution.

405 It is also interesting to investigate the effect of the first-order viscosity onto
 406 the steady-state solution. In Fig. 3, the steady-state velocity profile is plotted
 407 when using the first- and second-order viscosity coefficients: the main difference
 408 between the two numerical solution is in the resolution of the shock around

409 $x = 0.8m$. The first-order viscosity coefficient is by definition more dissipative
 410 and will smooth out the solution. In the other hand, the high-order viscosity
 411 better resolves the shock and allow high-order accuracy away from the shock
 412 region. It is also noted that the numerical solution obtained with the first-order
 413 viscosity coefficient is satisfying: this is due to the nature of the solution that
 414 contains a standing shock, and thus, will force the shock to form even with large
 415 artificial dissipation.

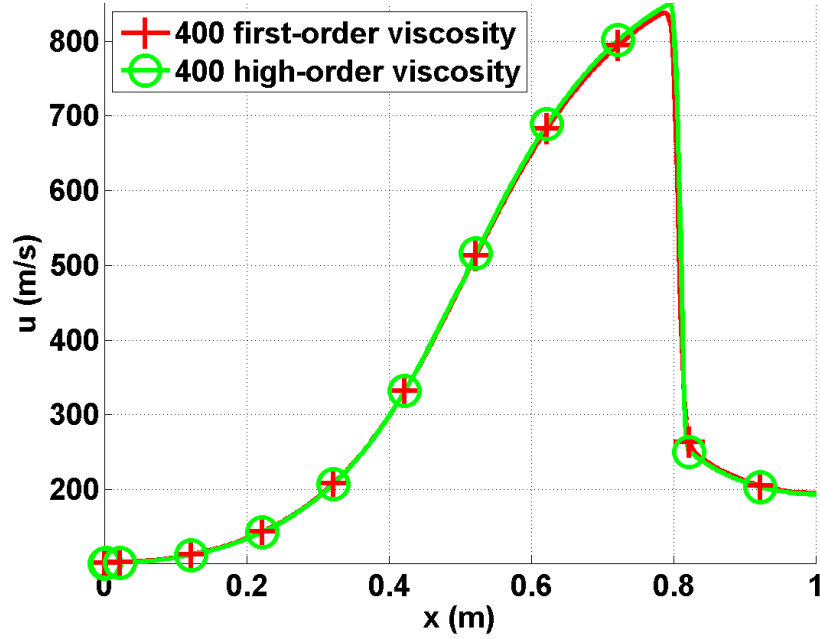


Figure 3: Velocity profile at steady-state with the first- and second-order viscosity for a mesh with 400 cells.

416 5.3. Leblanc shock tube

417 The 1-D Leblanc shock tube is a Riemann problem and designed to test the
 418 robustness and the accuracy of the stabilization method. The initial conditions
 419 are given in Table 7. The ideal gas equation of state is used to compute the
 420 fluid pressure with the following heat capacity ratio $\gamma = 5/3$.

Table 7: Initial conditions for the 1-D Leblanc shock tube.

	ρ	u	e
left	1.	0.	0.1
right	10^{-3}	0.	10^{-7}

421 This test is computationally challenging because of the large left to right
 422 pressure ratio. The computational domain consists of a 1-D pipe of length
 423 $L = 9m$ with an interface located at $x = 2m$. At $t = 0.s$, the interface is
 424 removed, allowing the fluid to move. The numerical solution is run until $t = 4.s$
 425 and the density, momentum and total energy profiles are given in Fig. 4a, Fig. 4b
 426 and Fig. 4c, respectively, along with the exact solution. The viscosity coefficients
 427 are also plotted in Fig. 4d. These plots were run with three different uniform
 428 mesh of 800, 3200 and 6000 cells and a constant time step $\Delta t = 10^{-3}s$.

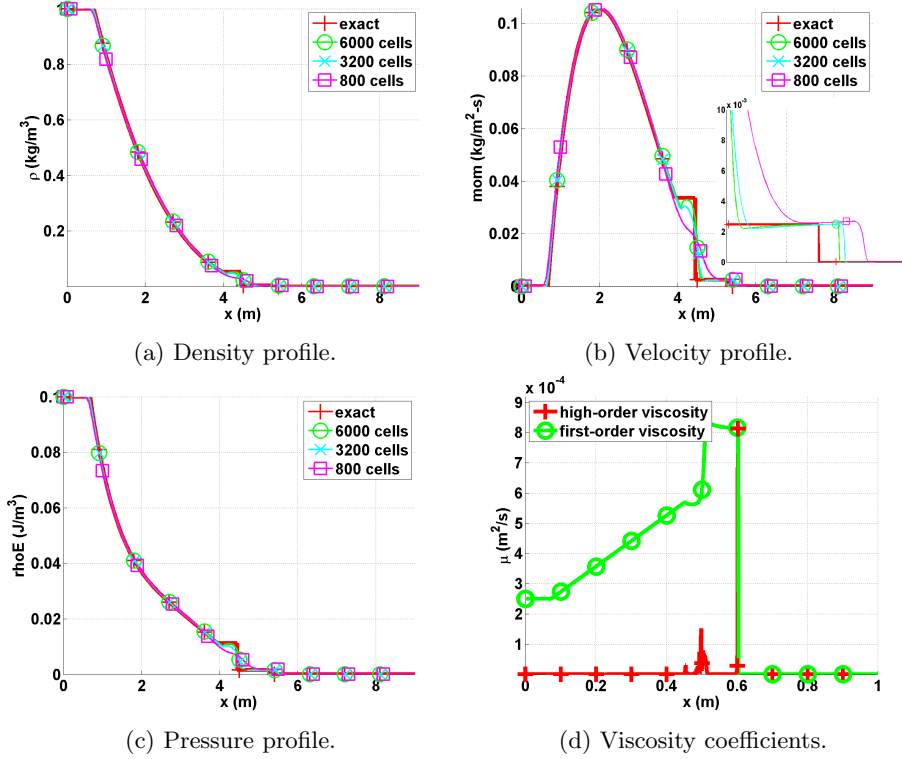


Figure 4: Numerical solution for the 1-D Leblanc shock tube at $t = 4.s$.

429 The density, momentum and total energy profiles given in Fig. 4 do not
 430 display any oscillations. In Fig. 4b, the shock region is zoomed in for better
 431 resolution: the shock is well resolved and do not show any oscillation. It is
 432 also observed that the shock position of the numerical solution converges to the
 433 exact position when refining the mesh. The contact wave is shown in Fig. 4b at
 434 $x = 4.5m$. The second-order viscosity coefficient profile is shown in Fig. 4d and
 435 behaves as expected: it saturates to the first-order viscosity in the shock region
 436 and thus prevent oscillations from forming. In the contact wave at $x = 4.5m$, a
 437 smaller peak is observed that is due to the presence of the jumps in the definition

438 of the second-order viscosity coefficient (Eq. (21)).
 439 Once again, a convergence study is performed in order to prove convergence of
 440 the numerical solution to the exact solution. As for the vapor phase in the 1-D
 441 nozzle (Section 5.2), the expected convergence rate for the L1 and L2 norms
 442 of the error are 1 and 1/2, respectively. The exact solution was obtained by
 443 running a 1-D Riemann solver and used as a reference solution to compute the
 444 L1 and L2-norms of the error that are reported in Table 8 and Table 9 for the
 445 conservative variables: density, momentum and total energy.

Table 8: L1 norm of the error for the 1-D Leblanc test at $t = 4.s$.

cells	density	rate	momentum	rate
100	$1.0354722 \cdot 10^{-2}$	—	$3.5471714 \cdot 10^{-3}$	—
200	$7.2680512 \cdot 10^{-3}$	0.51064841	$2.5933119 \cdot 10^{-3}$	0.45187331
400	$5.0825628 \cdot 10^{-3}$	0.51601245	$2.0668092 \cdot 10^{-3}$	0.32739054
800	$3.4025056 \cdot 10^{-3}$	0.57895861	$1.4793838 \cdot 10^{-3}$	0.48240884
1600	$2.1649953 \cdot 10^{-3}$	0.65223363	$9.7152832 \cdot 10^{-4}$	0.6066684
3200	$1.2465433 \cdot 10^{-3}$	0.79643094	$5.5937409 \cdot 10^{-4}$	0.79644263
6400	$6.4476928 \cdot 10^{-4}$	0.95107804	$3.0244198 \cdot 10^{-4}$	0.88715502
12800	$3.3950948 \cdot 10^{-4}$	0.92533116	$1.5958118 \cdot 10^{-4}$	0.9223679

cells	total energy	rate
100	0.0014033046	—
200	$9.8611746 \cdot 10^{-4}$	0.5089968
400	$7.7844421 \cdot 10^{-4}$	0.34116585
800	$5.5702549 \cdot 10^{-4}$	0.48285029
1600	$3.5720171 \cdot 10^{-4}$	0.64100438
3200	$2.0491799 \cdot 10^{-4}$	0.80169235
6400	$1.0914891 \cdot 10^{-4}$	0.90874889
12800	$5.7909794 \cdot 10^{-5}$	0.91441847

Table 9: L2 norm of the error for the 1-D Leblanc test at $t = 4.s$.

cells	density	rate	momentum	rate
100	$5.7187851 \cdot 10^{-3}$	—	$1.7767236 \cdot 10^{-3}$	—
200	$3.8995238 \cdot 10^{-3}$	0.55241073	$1.4913161 \cdot 10^{-3}$	0.25263314
400	$2.8103526 \cdot 10^{-3}$	0.4725468	$1.3305301 \cdot 10^{-3}$	0.164585
800	$2.1081933 \cdot 10^{-3}$	0.41474398	$1.1398931 \cdot 10^{-3}$	0.22310254
1600	$1.5731052 \cdot 10^{-3}$	0.42239201	$9.0394227 \cdot 10^{-4}$	0.33459602
3200	$1.0610667 \cdot 10^{-3}$	0.56809979	$6.2735595 \cdot 10^{-4}$	0.52694639
6400	$7.3309974 \cdot 10^{-4}$	0.53343397	$4.4545754 \cdot 10^{-4}$	0.49399631
12800	$5.1020991 \cdot 10^{-4}$	0.52291857	$3.1266758 \cdot 10^{-4}$	0.5106583

cells	total energy	rate
100	$7.6112265 \cdot 10^{-4}$	—
200	$5.5497308 \cdot 10^{-4}$	0.45571115
400	$4.6063172 \cdot 10^{-4}$	0.26880405
800	$3.7798953 \cdot 10^{-4}$	0.28526749
1600	$2.9584646 \cdot 10^{-4}$	0.35349763
3200	$2.054455 \cdot 10^{-4}$	0.52609289
6400	$1.4670834 \cdot 10^{-4}$	0.48580482
12800	$1.0299897 \cdot 10^{-5}$	0.51032105

The convergence rates are close to the expected values which prove convergence of the numerical solution to the exact solution.

5.4. Subsonic flow over a 2-D cylinder

The flow of a fluid over a 2-D cylinder is a typical benchmark case to test the behavior of a numerical method in the low Mach regime. For this test, an analytical solution is available in the incompressible limit or low Mach limit (REFS) and often referred to as potential flow. The numerical solution can be compared against the analytical solution in order to evaluate the effect of the numerical dissipation. The main features of the potential flow are the following:

- The solution is symmetric: the iso-mach number lines are used to assess the symmetry of the numerical solution.
- The velocity at the top of the cylinder is twice the incoming velocity set at the inlet.
- The pressure fluctuations are proportional to the inlet Mach number square, as follows:

$$\tilde{P} = \frac{\max(P) - \min(P)}{\max(P)} \propto M_{\infty}^2$$

where \tilde{P} and M_{∞} are the pressure fluctuations and the inlet Mach number, respectively.

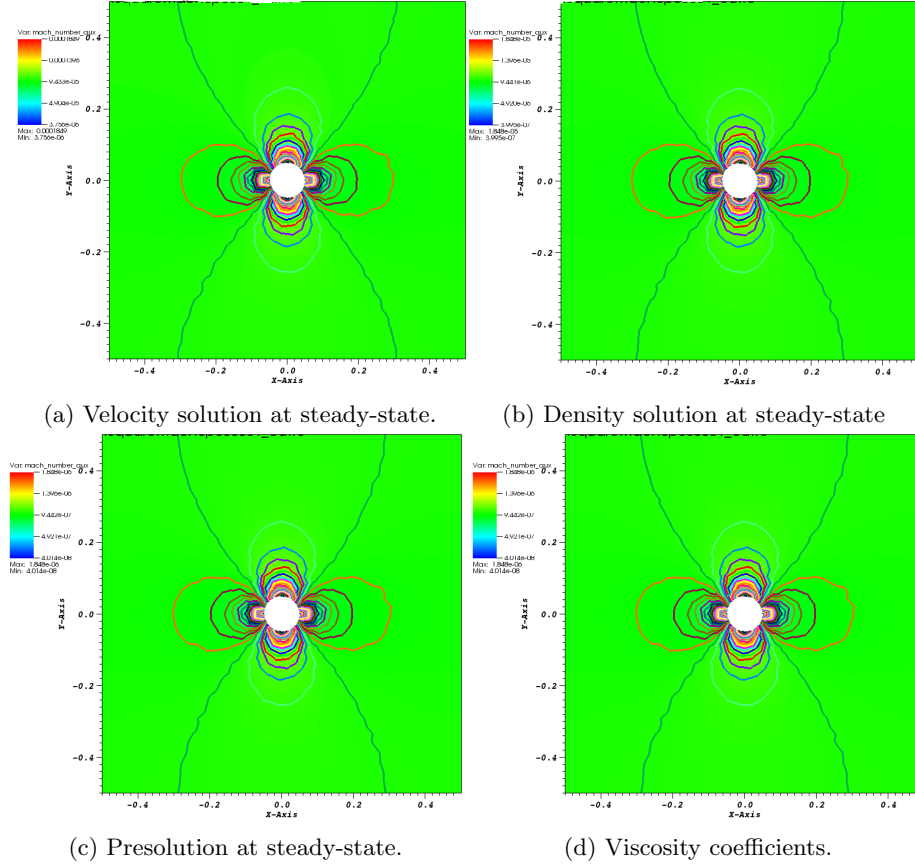


Figure 5: Steady-state solution for vapor phase in a 1-D convergent-divergent nozzle.

5.5. Subsonic flow over a 2-D hump

This is a another example of an internal flow configuration. It consist of a channel of height $L = 1\text{ m}$ and length $3L$, with a circular bump of length L and thickness $0.1L$. The bump is located on the bottom wall at a distance L from the inlet. The system is initialized with an uniform pressure $P = 101325\text{ Pa}$ and temperature $T = 300\text{ K}$. The initial velocity is computed from the Mach number, M , the pressure, the temperature and the Ideal Gas equation of state with the heat capacity $C_v = 717\text{ J/kg} - \text{K}$ and the heat capacity ratio $\gamma = 1.4$. At the inlet, a subsonic stagnation boundary condition is used: the stagnation pressure and temperature are computed using the following relations, valid for the Stiffened and Ideal gas equation of states:

$$\begin{cases} P_0 = P \left(1 + \frac{\gamma-1}{2} M^2\right)^{\frac{\gamma}{\gamma-1}} \\ T_0 = T \left(1 + \frac{\gamma-1}{2} M^2\right) \end{cases} \quad (27)$$

474 The static pressure $P_s = 101325 \text{ Pa}$ is set at the subsonic outlet. An uniform
 475 grid is used to get the numerical solution until steady-state is reached. The
 476 results are shown in Fig. 6a, Fig. 6b, Fig. 6c and Fig. 6d for the inlet Mach
 477 numbers $M = 0.7$, $M = 0.01$, $M = 10^{-4}$ and $M = 10^{-7}$, respectively. It
 478 is expected that, within the low Mach number range, the solution does not
 479 depend on the Mach number and is identical to the solution obtained with
 480 an incompressible flow code. On the other hand, for a flow at $M = 0.7$, the
 481 compressible effects become more important and shock can form.

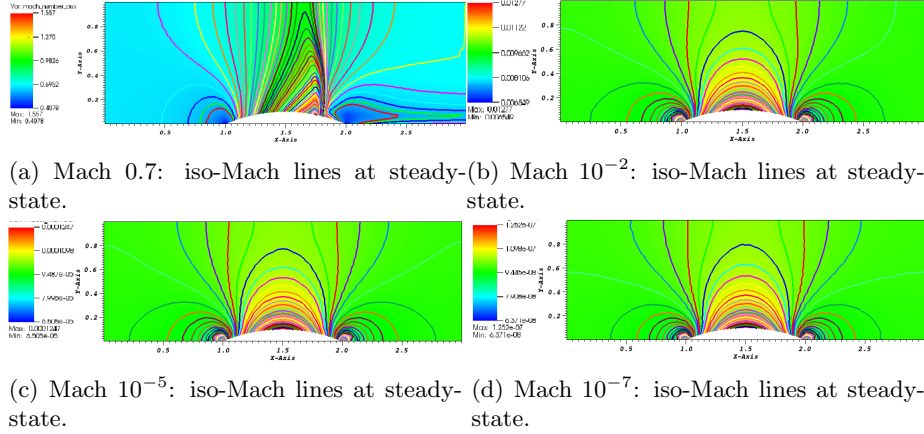


Figure 6: Steady-state solution for a 2-D flow over a circular bump.

482 The results showed in Fig. 6b, Fig. 6c and Fig. 6d correspond to the low
 483 Mach regime. The iso-Mach lines are drawn ranging from the minimum and the
 484 maximum of each legend with 50 intervals. The steady-state solution is sym-
 485 metric and does not depend on the value of the inlet Mach number as expected.
 486 In Fig. 6a, the steady-state numerical solution develops a shock: the compress-
 487 ibility effect are no longer negligible. The iso-Mach lines are also plotted with
 488 50 intervals and ranging from 0.4 to 1.6. The shock is well resolved and does
 489 not display any instability or spurious oscillation.
 490 The results presented in Fig. 6 were obtained with the new definition of the vis-
 491 cosity coefficient (see Eq. (21)), and, illustrate the capabilities of the entropy-
 492 viscosity method to adapt to the type of flow (subsonic and transonic flows)
 493 without using any tuning parameters, but by just evaluating the entropy resid-
 494 ual that is an indicator of the entropy production.

5.6. Supersonic flow in a compression corner

496 This is an example of a supersonic flow over a wedge of angle 15° : an oblique
 497 shock is generated at steady-state. The Mach number upstream of the shock
 498 is fixed to $M = 2.5$. The initial conditions are uniform: the pressure and
 499 temperature are set to $P = 101325 \text{ Pa}$ and $T = 300 \text{ K}$, respectively. The
 500 velocity is computed from the upstream Mach number and using the Ideal Gas

501 equation of state with the same parameters as in Section 5.5. The code is run
 502 until steady-state. An analytical solution for this supersonic flow is available
 503 and give the downstream to upstream pressure, entropy and Mach number ratios
 504 (REF). The analytical and numerical ratios are given in see in Table 10.

Table 10: Analytical solution for the supersonic flow on an edge eat 15° at $M = 2.5$.

	analytical downstream to upstream ratio	numerical downstream to upstream ratio
Pressure	2.47	
Mach number	0.74	
Entropy	1.03	

505 The inlet is supersonic and therefore, the pressure, temperature and velocity
 506 have to be specified using Dirichlet boundary conditions. The outlet remains
 507 subsonic and only the back pressure is set to $P_b = 101325 \text{ Pa}$.

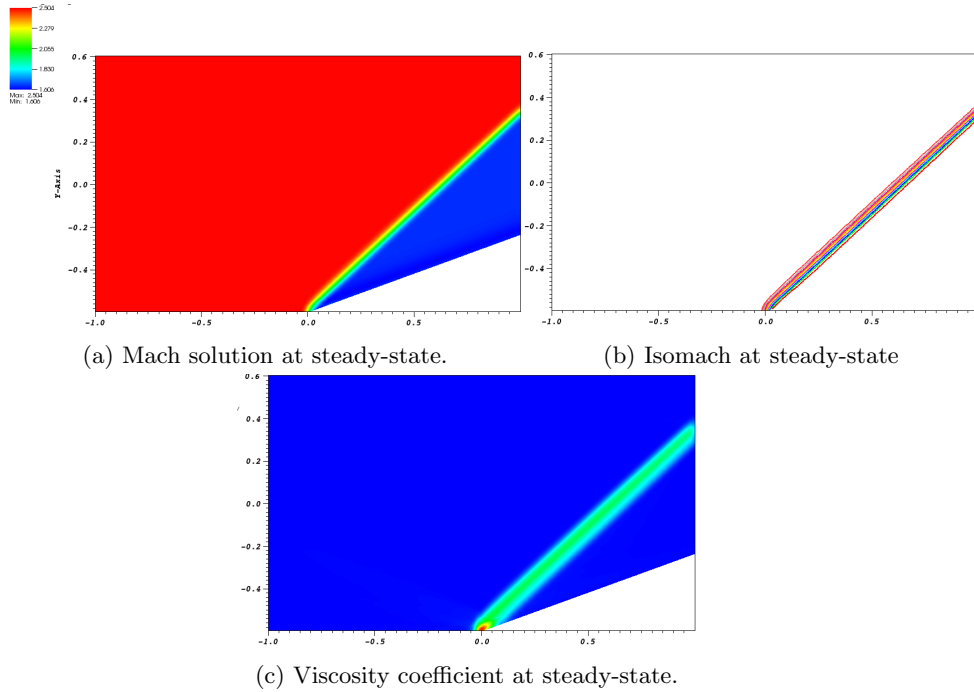


Figure 7: Steady-state solution for a flow in a 2-D compression corner.

508 The steady-state numerical solution is given in Eq. (7): the Mach number,
 509 the iso-Mach lines and the viscosity coefficients are plotted in Fig. 7a, Fig. 7b

and Fig. 7c, respectively. The steady-state solution is formed of two regions of constant states, separated by the oblique shock. The iso-Mach lines (see Fig. 7b) range from 1.6 to 2.5 with 20 intervals. In Fig. 7c, the viscosity coefficient is large in the shock, small anywhere else, and thus, behaves as expected. At the corner of the edge at $x = 0.0\text{ m}$, the viscosity coefficient is peaked because of the treatment of the wall boundary condition: at this particular node, the normal is not well defined and can cause numerical errors. Overall, the numerical solution does not show any oscillations and match the analytical solution, and the shock is well resolved.

6. Conclusions

Acknowledgments

References

- [1] R. P. J-L. Guermond, Entropy viscosity method for nonlinear conservation laws, *Journal of Comput. Phys* 230 (2011) 4248–4267.
- [2] R. P. J-L. Guermond, Entropy viscosity method for high-order approximations of conservation laws, *Lecture Notes in Computational Science and Engineering* 76 (2011) 411–418.
- [3] R. P. J-L. Guermond, Entropy-based nonlinear viscosity for fourrier approximations of conservation laws, in: *C.R. Math. Acad. Sci.*, Vol. 326, Paris, 2008, pp. 801–806.
- [4] J. M. V. Zingan, J-L. Guermond, B. Popov, Implementation of the entropy viscosity method with the discontinuous galerkin method, *Berlin: Springer* 253 (2013) 479–490.
- [5] J.-L. Guermond, B. Popov, Viscous regularization of the euler equations and entropy principles, under review.
- [6] P. B., S. C-W., On positivity preserving finite volume schemes for euler equations, *Numer. Math.* 73 (1996) 119–130.
- [7] E. Toro, *Riemann Solvers and numerical methods for fluid dynamics*, 2nd Edition, Springer, 1999.
- [8] O. L. R. Berry, R. Saurel, The discrete equation method (dem) for fully compressible, two-phase flows in ducts of spatially varying cross-section, *Nuclear Engineering and Design* 240 (2010) 3797–3818.